

CLIP-aware Domain-Adaptive Super-Resolution

Zhengyang Lu¹, Qian Xia², Weifan Wang¹ and Feng Wang^{1*}

¹ Jiangnan University, China

² Changshu Institute of Technology, China

Abstract—This work introduces CLIP-aware Domain-Adaptive Super-Resolution (CDASR), a novel framework that addresses the critical challenge of domain generalization in single image super-resolution. By leveraging the semantic capabilities of CLIP (Contrastive Language-Image Pre-training), CDASR achieves unprecedented performance across diverse domains and extreme scaling factors. The proposed method integrates CLIP-guided feature alignment mechanism with a meta-learning inspired few-shot adaptation strategy, enabling efficient knowledge transfer and rapid adaptation to target domains. A custom domain-adaptive module processes CLIP features alongside super-resolution features through a multi-stage transformation process, including CLIP feature processing, spatial feature generation, and feature fusion. This intricate process ensures effective incorporation of semantic information into the super-resolution pipeline. Additionally, CDASR employs a multi-component loss function that combines pixel-wise reconstruction, perceptual similarity, and semantic consistency. Extensive experiments on benchmark datasets demonstrate CDASR’s superiority, particularly in challenging scenarios. On the Urban100 dataset at $\times 8$ scaling, CDASR achieves a significant PSNR gain of 0.15dB over existing methods, with even larger improvements of up to 0.30dB observed at $\times 16$ scaling.

Index Terms—Image super-resolution, domain adaptation, Contrastive Language-Image Pre-training, meta-learning

I. INTRODUCTION

Single-image super-resolution (SISR) advances the development of image reconstruction techniques, as the frontier challenge in the low-level computer vision field [1]–[3]. SISR has become a critical component in fields as diverse as medical diagnostics, where it enhances the clarity of MRI scans [4], to space exploration, where it sharpens satellite imagery of distant planets [5]. Deep learning has catapulted SISR into a new benchmark, with convolutional neural networks (CNNs) and transformers achieving unprecedented levels of detail recovery [6]–[8]. These advancements have not only improved image quality metrics but have also facilitated facial recognition [9], forensic image analysis [10], and the preservation of cultural heritage through the restoration of historical photographs [11]–[13]. However, as resolution enhancement techniques approach theoretical limits, a fundamental tension emerges: the trade-off between computational efficiency and the quality of reconstructed images. The deeper exploration of super-resolution uncovers questions that challenge current understanding of image formation, perception, and the very nature of visual information itself [14], [15].

Figure 1 illustrates the 2D t-SNE visualization of CLIP features across various super-resolution datasets. The distribution

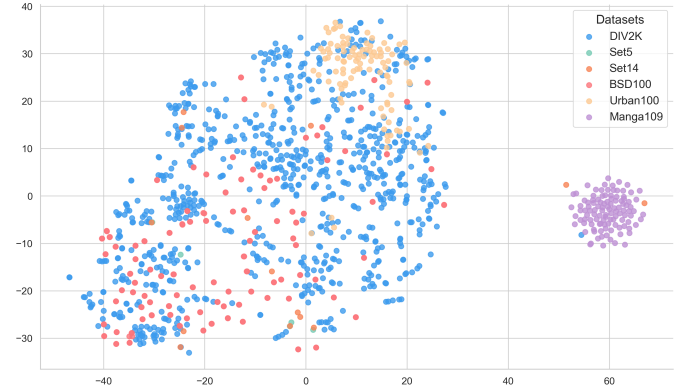


Fig. 1. 2D t-SNE visualization of CLIP features extracted from various super-resolution benchmark datasets. DIV2K (blue) shows a wide distribution covering multiple domains, BSD100 (red) clusters predominantly in one region with partial overlap with DIV2K, while Manga109 (purple) forms a distinctly separate cluster due to its unique anime-style content. This distribution highlights the significant domain differences that super-resolution models must address.

reveals interesting patterns in how these datasets relate in feature space. DIV2K exhibits a wide distribution range, partially encompassing Urban100 features in one region, indicating some shared characteristics between these datasets. However, Manga109 forms a distinctly separate cluster due to its unique anime-style content, which differs significantly in visual semantics from photographic images. Even within the seemingly closer clusters, subtle separations are visible between dataset features, suggesting domain-specific characteristics that may impact super-resolution performance. This visualization provides evidence that semantic feature distributions vary across datasets, with the degree of variation potentially influencing how well super-resolution models generalize across domains. While some domains show greater similarity (DIV2K and Urban100), others represent more challenging transfer learning scenarios (Manga109), underscoring the need for domain-adaptive approaches in super-resolution tasks.

To address these challenges, we propose CLIP-aware Domain-Adaptive Super-Resolution (CDASR), a novel framework that leverages the semantic understanding capabilities of CLIP (Contrastive Language-Image Pre-training) to enhance domain adaptation in SISR. Our approach integrates a CLIP-guided feature alignment mechanism with a meta-learning inspired few-shot adaptation strategy, enabling efficient knowledge transfer across diverse image domains. The CLIP-guided feature alignment utilizes the rich semantic representations learned by pre-trained CLIP models to bridge the domain gap

between source and target datasets. This alignment is achieved through a custom domain-adaptive module that processes CLIP features alongside super-resolution features, facilitating effective cross-domain knowledge transfer. The module employs a multi-stage transformation process, including CLIP feature processing through a multi-layer perceptron, spatial feature generation via convolutional layers, and feature fusion with the original super-resolution features. This intricate process ensures that the semantic information captured by CLIP is effectively incorporated into the super-resolution pipeline, allowing for generalizable reconstructions. Additionally, the framework incorporates a novel multi-component loss function that combines pixel-wise reconstruction, perceptual similarity, and semantic consistency, further enhancing the model's ability to preserve low-level details and high-level semantic information across diverse image domains.

Furthermore, we introduce a meta-learning inspired few-shot adaptation technique that allows our model to quickly adapt to target domains using only a few labelled examples. This approach leverages a meta-objective that optimizes for rapid adaptation across multiple domains, resulting in a flexible super-resolution model. The combination of CLIP-guided alignment and meta-learning enables CDASR to achieve state-of-the-art performance across multiple scaling factors, while requiring minimal fine-tuning for target domains.

Our experimental results demonstrate the effectiveness of CDASR across multiple benchmark datasets and scaling factors. On the challenging Urban100 dataset at $\times 8$ scaling, CDASR achieves a PSNR gain of 0.15dB over the next best method, with even larger improvements of up to 0.30dB observed at $\times 16$ scaling. These results highlight the robustness of our approach on extreme upscaling scenarios.

The main contributions of this work are summarized as follows:

- We propose CDASR, a CLIP-aware domain-adaptive super-resolution framework that integrates CLIP's semantic representations with super-resolution features to enhance cross-domain generalization in SISR tasks.
- We introduce a CLIP-guided feature alignment mechanism with a multi-component loss function, ensuring both low-level fidelity and high-level semantic coherence across diverse domains.
- We develop a meta-learning inspired few-shot adaptation strategy, enabling rapid adaptation to new domains with minimal samples through adaptive learning rate modulation.

Despite these promising results, CDASR faces challenges with extremely complex scenes involving reflections and semantic anomalies. Future work should focus on developing more advanced semantic parsing techniques and exploring the integration of temporal information for video super-resolution applications.

II. RELATED WORKS

SISR has been a longstanding challenge in computer vision, aiming to reconstruct high-resolution (HR) images from their low-resolution (LR) counterparts. This section provides an

overview of recent advancements in deep learning-based SR methods, focusing on CNN and transformer-based approaches.

A. CNN-based Super-Resolution

Deep learning has revolutionized the field of SISR. Early CNN-based methods like SRCNN [16] and VDSR [17] demonstrated the potential of deep learning for SISR. Subsequent research explored increasingly sophisticated architectures to enhance performance. Lim et al. proposed EDSR [18], which significantly improved results by optimizing residual network structures for SR. The introduction of attention mechanisms marked another significant advancement. Zhang et al. developed RCAN [19], incorporating channel attention to adaptively re-calibrate feature responses. This concept was further extended in HAN [20], which explored multi-scale attention across channels, layers, and spatial locations. Lu et al. proposed UnetSR [21], adapting the U-Net architecture [22] for SR tasks with a mixed gradient loss.

Recognizing the limitations of local convolutions, researchers began investigating methods to capture long-range dependencies. Zhou et al. introduced IGNN [23], leveraging graph neural networks to model cross-scale patch recurrence. Dai et al. proposed SAN [24], employing second-order attention to enhance feature correlations. These approaches demonstrated the importance of non-local information in SR tasks. Mei et al. presented NLSA [25], combining non-local operations with sparse representation to balance global modeling capability and computational efficiency.

Recent works focused on developing lightweight SR models to address practical deployment constraints. Li et al. proposed LAPAR [26], employing a linearly-assembled pixel-adaptive regression approach. Luo et al. introduced LatticeNet [27], utilizing an efficient lattice block structure. Lu et al. developed DenseSR [28], introducing a dense U-Net with shuffle pooling layer. These efforts highlight the ongoing challenge of balancing model complexity and performance in real-world SR applications.

B. Transformer-based Super-Resolution

The success of transformer architectures in natural language processing has inspired their adoption in computer vision tasks, including SR. Liang et al. introduced SwinIR [29], adapting the Swin Transformer for image restoration. This shift towards transformer-based models represents a promising direction for overcoming the inherent limitations of CNNs in capturing long-range dependencies. Building on this foundation, Chen et al. proposed IPT [30], a pre-trained transformer model that demonstrates excellent performance across various low-level vision tasks. Lu et al. introduced EDT [31], exploring efficient transformer-based image pre-training specifically tailored for low-level vision tasks. Swin-FIR [32] further refined the transformer-based approach by incorporating frequency domain information, while HAT [33] introduced a hybrid attention transformer to balance local and global feature interactions.

Recent advancements have focused on optimizing transformer architectures for SR tasks. ESRT [34] introduced

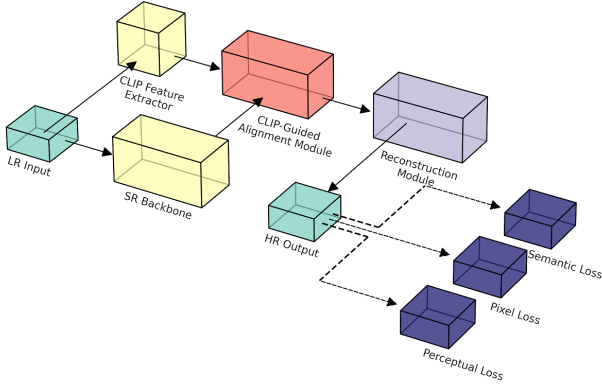


Fig. 2. Overview of the proposed CDASR framework. The CLIP-guided alignment module (a) fuses semantic information from CLIP with SR features, while the reconstruction module (b) generates the final high-resolution output.

an efficient transformer structure that leverages multi-scale feature fusion. Hsu et al. proposed DRCT [35], a dense-residual-connected transformer that mitigates information bottlenecks in SR tasks through enhanced feature preservation and information flow stabilization. These approaches demonstrate the potential of transformer-based models to achieve state-of-the-art performance while addressing computational efficiency concerns.

Modern advances in semantic-based approaches have shown promise for domain generalization. Liu et al. [36] proposed a domain-agnostic expert framework for person re-identification that transfers knowledge across unlabeled domains. Similarly, Chen et al. [37] introduced a conjugated semantic pool that improves out-of-distribution detection with pre-trained vision-language models. These works validate the effectiveness of semantic guidance for cross-domain generalization, aligning with our CLIP-based approach.

III. PROPOSED METHOD

To address the challenges of domain-adaptive super-resolution, we propose a novel framework that leverages CLIP’s semantic understanding capabilities. Our method consists of three key components: a CLIP-guided feature alignment module, a domain-adaptive reconstruction network, and a meta-learning inspired few-shot adaptation strategy. This section details each component and their integration within the overall framework, providing insights into how they collectively enhance cross-domain generalization in single image super-resolution tasks.

A. Overview

Let $\mathcal{D}_s = \{(x_i^s, y_i^s)\}_{i=1}^{N_s}$ denote the source domain dataset used to pre-train our super-resolution model, where x_i^s and y_i^s represent low-resolution (LR) and high-resolution (HR) image pairs, respectively. Our goal is to adapt this model to K target domains $\{\mathcal{D}_t^k\}_{k=1}^K$, each with a distinct scene, using only a few labeled examples per domain. We denote the few-shot target domain datasets as $\mathcal{D}_t^k = \{(x_i^{t,k}, y_i^{t,k})\}_{i=1}^{N_t^k}$, where $N_t^k \ll N_s$.

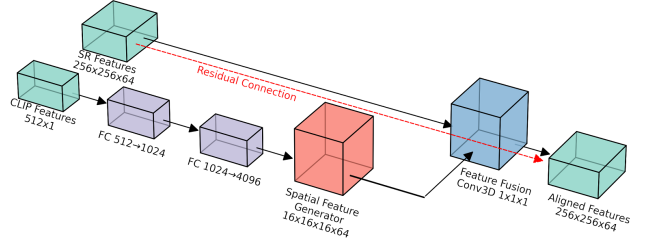


Fig. 3. CLIP-guided alignment module fusing semantic and spatial information for enhanced super-resolution.

In Figure 2, the CDASR framework operates in multiple stages. At first, the low-resolution input is simultaneously processed by the CLIP feature extractor (E_{CLIP}) and the super-resolution backbone (F_θ). The extracted CLIP features and super-resolution features are then fused in the CLIP-Guided Alignment Module (G_ϕ), which adapts the features to the target domain. The aligned features are subsequently fed into the reconstruction module R_ψ to generate the high-resolution output. The entire process is optimized using a combination of perceptual, pixel-wise, and semantic loss functions, ensuring both low-level fidelity and high-level semantic consistency in the super-resolved images across diverse domains.

B. CLIP-Guided Feature Alignment

To efficiently introduce semantic information into super-resolution, we propose a novel CLIP-guided feature alignment mechanism. This approach leverages the rich semantic representations learned by pre-trained CLIP models to facilitate effective cross-domain knowledge transfer.

The CLIP-guided alignment module, illustrated in Figure 3, integrates CLIP features with SR features through a sophisticated multi-stage process. Initially, CLIP features undergo a fully connected operation to reshape them into a spatial format. These spatially-aligned features are then processed through 3D convolutions. Simultaneously, the original SR features flow through a parallel path. The two streams converge in a fusion step, where the processed CLIP features are combined with the SR features. To further enhance information preservation, a residual connection reintroduces the original SR features. This intricate architecture culminates in the production of aligned features that effectively incorporate both semantic and spatial information.

This design leverages CLIP’s semantic understanding while preserving spatial information crucial for super-resolution. The multi-stage approach allows for gradual integration of semantic and spatial features, potentially mitigating information loss. The residual connection ensures that fine-grained details from the original SR features are not overlooked, striking a balance between semantic enrichment and detail preservation.

1) *CLIP Feature Extraction*: We apply a fixed pre-trained CLIP model to extract domain-agnostic semantic features from both source and target domain images. The CLIP model, developed by Radford et al. [38], has demonstrated remarkable zero-shot transfer capabilities across various vision tasks. In

the proposed framework, we specifically employ the vision encoder of CLIP, which remains frozen throughout our training process.

Given an image I , we define the CLIP feature extraction process as:

$$f_{\text{CLIP}}(I) = E_{\text{CLIP}}(I) / |E_{\text{CLIP}}(I)|_2 \quad (1)$$

where E_{CLIP} is the fixed CLIP image encoder, and $|\cdot|_2$ denotes L2 normalization. These normalized CLIP features capture high-level semantic information that is largely invariant to low-level domain-specific characteristics.

2) *Domain-Adaptive Feature Alignment Module*: We introduce a domain-adaptive alignment module G_ϕ to align feature distributions across domains. This module processes CLIP features f_{CLIP} and super-resolution features $F_\theta(x)$ through multi-stage transformations:

$$G_\phi : [F_\theta(x), f_{\text{CLIP}}(x)] \rightarrow \mathbb{R}^d \quad (2)$$

where d is the aligned feature space dimension. The module consists of three key components: CLIP feature processing, spatial feature generation, and feature fusion.

The CLIP feature processor transforms the input CLIP features through a two-layer MLP with ReLU activation:

$$f_{\text{proc}} = \text{ReLU}(W_2 \cdot \text{ReLU}(W_1 \cdot f_{\text{CLIP}} + b_1) + b_2) \quad (3)$$

where $W_1 \in \mathbb{R}^{h \times c}$, $W_2 \in \mathbb{R}^{s \times h}$, with hidden dimension $h = 1024$ and output dimension $s = 512$. The processed features are then expanded spatially and passed through convolutional layers to generate spatial features:

$$f_{\text{spatial}} = \text{Conv}_2(\text{ReLU}(\text{Conv}_1(f_{\text{proc}}))) \quad (4)$$

Finally, these spatial features are fused with the original super-resolution features:

$$f_{\text{aligned}} = \text{ConvFusion}([F_\theta(x), f_{\text{spatial}}]) \quad (5)$$

This architecture enables effective domain adaptation by leveraging CLIP's semantic understanding while preserving spatial information crucial for super-resolution tasks. The use of residual connections and layer normalization further enhances feature propagation and stability during training.

3) *Training Objective*: We employ a multi-component loss function to train the novel alignment module and the super-resolution model:

$$\mathcal{L}_{\text{total}} = \lambda_{\text{pixel}} \mathcal{L}_{\text{pixel}} + \lambda_{\text{perc}} \mathcal{L}_{\text{perc}} + \lambda_{\text{sem}} \mathcal{L}_{\text{sem}} \quad (6)$$

where $\mathcal{L}_{\text{pixel}}$ is the pixel-wise L1 loss, $\mathcal{L}_{\text{perc}}$ is the perceptual loss [39], and \mathcal{L}_{sem} is the semantic consistency loss. The semantic consistency loss is defined as:

$$\mathcal{L}_{\text{sem}} = |f_{\text{CLIP}}(F_\theta(x_{LR})) - f_{\text{CLIP}}(x_{HR})|_2^2 \quad (7)$$

This loss function encourages the model to generate high-resolution images that are not only close to the target at the pixel level but also consistent in terms of higher-level semantic features.

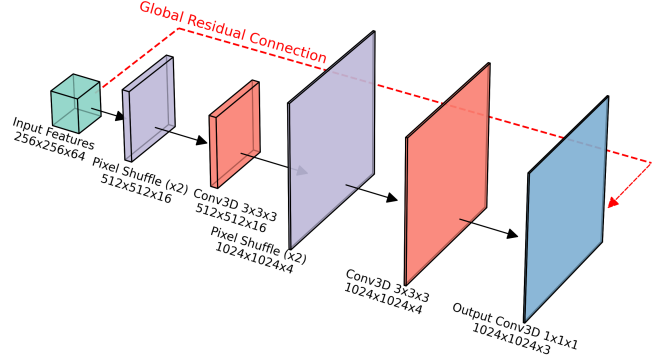


Fig. 4. Reconstruction module architecture for generating high-resolution output from aligned features.

4) *Reconstruction Module*: The reconstruction module serves as the final stage in CDASR framework, responsible for generating the high-resolution output. As shown in Figure. 4, this module consists of a multi-stage upsampling layers followed by convolutional operations. The module takes the aligned features from the feature alignment module as input and progressively increases the spatial resolution while refining the details. The residual connection facilitate the learning of high-frequency information.

The architecture of the reconstruction module is designed to be scale-aware, adapting its structure based on the target upscaling factor. For $\times 2$ and $\times 4$ upscaling, we use a cascade of pixel shuffle layers, each followed by a 3×3 convolutional layer. For $\times 8$ and higher factors, we introduce an additional set of residual blocks between upsampling stages to enhance the model's capacity for detail synthesis. The final output is generated through a global residual connection, combining the upscaled features with the initial bicubic interpolation of the input, ensuring stability in training and preservation of low-frequency content.

C. Optimization Procedure

1) *Training Objective*: We employ a multi-component loss function to train the enhanced alignment module and the super-resolution model:

$$\mathcal{L}_{\text{total}} = \mathcal{L}_1 + \lambda_{\text{perc}} \mathcal{L}_{\text{perc}} + \lambda_{\text{sem}} \mathcal{L}_{\text{sem}} \quad (8)$$

where \mathcal{L}_1 is the standard pixel-wise L1 loss, $\mathcal{L}_{\text{perc}}$ is the perceptual loss, and \mathcal{L}_{sem} is the novel Multi-Scale Semantic Consistency Loss.

The CLIP-based semantic consistency loss \mathcal{L}_{sem} is defined as:

$$\mathcal{L}_{\text{sem}} = \|f_{\text{CLIP}}(F_\theta(x_{LR})) - f_{\text{CLIP}}(x_{HR})\|_2^2 \quad (9)$$

where x_{LR} and x_{HR} are the low-resolution and high-resolution images respectively, F_θ is the super-resolution model, and f_{CLIP} is the CLIP feature extractor.

The purpose of this loss function is to minimize the distance between the super-resolution result and the true high-resolution

image in the CLIP feature space, thereby ensuring semantic consistency throughout the super-resolution process. By doing so, we encourage the model to generate high-resolution images that are not only close to the target at the pixel level but also consistent in terms of higher-level semantic features.

The training process of the proposed CDASR framework consists of three main stages: pre-training, CLIP-guided alignment, and meta-learning. The inference process involves adapting the model to heterogeneous target domains using few-shot samples. Algorithm 1 provides a detailed description of our training and inference procedures.

2) *Training and Inference*: The training and inference procedures for the proposed CDASR framework are detailed in Algorithm 1. We show the algorithm to reflect the implementation steps:

Algorithm 1 CDASR Training Procedure

Require: Source domain dataset \mathcal{D}_s , CLIP model E_{CLIP}

Ensure: Optimized super-resolution model for source domains

```

1: function TRAIN( $\mathcal{D}_s, E_{\text{CLIP}}$ )
2: Initialize super-resolution backbone  $F_\theta$ 
3: Initialize domain-adaptive alignment module  $G_\phi$ 
4: Initialize reconstruction module  $R_\psi$ 
5: Initialize meta-learner  $M$ 
6: Initialize optimizer with learning rate  $\eta$ 
7: Initialize learning rate scheduler
8: for  $epoch = 1$  to  $N_{\text{epochs}}$  do
9:   for each batch  $(x_{LR}, x_{HR})$  in  $\mathcal{D}_s$  do
10:    Extract CLIP features:  $f_{\text{CLIP}} = E_{\text{CLIP}}(x_{LR})$ 
11:    Compute SR features:  $f_{SR} = F_\theta(x_{LR})$ 
12:    Compute aligned features:
13:       $f_{\text{aligned}} = G_\phi([f_{SR}, f_{\text{CLIP}}])$ 
14:    Generate SR images:  $x_{SR} = R_\psi(f_{\text{aligned}})$ 
15:    Compute  $\mathcal{L}_{\text{total}} = \mathcal{L}_1 + \lambda_{\text{perc}}\mathcal{L}_{\text{perc}} + \lambda_{\text{sem}}\mathcal{L}_{\text{sem}}$ 
16:    Update  $F_\theta$ ,  $G_\phi$ , and  $R_\psi$  by minimizing  $\mathcal{L}_{\text{total}}$ 
17:   end for
18:   Update learning rate using scheduler
19: end for
```

The training procedure of the proposed CDASR framework consists of three main stages: pre-training, CLIP-guided alignment, and meta-learning. Algorithm 1 provides a detailed description of our training and inference procedures. During training, we initialize the super-resolution backbone F_θ , the domain-adaptive alignment module G_ϕ , the reconstruction module R_ψ , and the meta-learner M . For each batch, we extract CLIP features, compute super-resolution features, align these features using G_ϕ , and generate super-resolved images using the reconstruction module R_ψ . The model is updated by minimizing a multi-component loss function that includes L1 loss, perceptual loss, and semantic consistency loss.

3) *Meta-Learning-based Few-Shot Adaptation*: We propose a meta-learning inspired few-shot adaptation strategy that complements the CLIP-guided alignment for efficient adaptation to new target domains [40]. This approach is applied during the ADAPT function in Algorithm 1, allowing the model to

leverage both general semantic knowledge and domain-specific information efficiently.

To enhance the efficiency of few-shot adaptation, we introduce an adaptive learning rate modulation scheme within the ADAPT function, following principles of meta-transfer learning [41]. For each parameter θ_i in the model (including F_θ , G_ϕ , and R_ψ), we learn a corresponding meta-learning rate α_i that determines the adaptability:

$$\theta'_i = \theta_i - \alpha_i \nabla_{\theta_i} \mathcal{L}_{\mathcal{D}_t^k}(\theta) \quad (10)$$

where $\mathcal{L}_{\mathcal{D}_t^k}$ is the loss computed on the support set \mathcal{S} from the new target domain \mathcal{D}_t^k .

The meta-learning rates α_i are updated using the meta-objective:

$$\alpha_i \leftarrow \alpha_i - \gamma \frac{\partial}{\partial \alpha_i} \mathcal{L}_Q(\theta') \quad (11)$$

where γ is a higher-order learning rate, and \mathcal{L}_Q is the loss computed on the query set \mathcal{Q} from the target domain.

This adaptive scheme allows the model to learn which parameters should be more plastic during few-shot adaptation, leading to effective domain transfer without affecting the original training process.

Algorithm 2 CDASR Adaptation Procedure

```

1: function ADAPT( $F_\theta, G_\phi, R_\psi, \mathcal{D}_t^{\text{new}}, E_{\text{CLIP}}$ )
2: Initialize meta-learner  $M$  with current model parameters
3: for  $episode = 1$  to  $N_{\text{episodes}}$  do
4:   Sample support set  $\mathcal{S}$  and query set  $\mathcal{Q}$  from  $\mathcal{D}_t^{\text{new}}$ 
5:    $\theta', \phi', \psi' = M.\text{adapt}(\mathcal{S}, F_\theta, G_\phi, R_\psi)$ 
6:   for each batch  $(x_{LR}, x_{HR})$  in  $\mathcal{Q}$  do
7:     Extract CLIP features:  $f_{\text{CLIP}} = E_{\text{CLIP}}(x_{LR})$ 
8:     Compute SR features:  $f_{SR} = F_{\theta'}(x_{LR})$ 
9:     Compute aligned features:
10:       $f_{\text{aligned}} = G_{\phi'}([f_{SR}, f_{\text{CLIP}}])$ 
11:     Generate SR images:  $x_{SR} = R_{\psi'}(f_{\text{aligned}})$ 
12:     Compute loss  $\mathcal{L}$  on  $(x_{SR}, x_{HR})$ 
13:     Update  $M$  using  $\mathcal{L}$  and MAML or Reptile algorithm
14:   end for
15: end for
16: return Adapted  $F_{\theta'}, G_{\phi'}, R_{\psi'}$ 
```

Algorithm 2 outlines the adaptation procedure for CDASR. It initializes a meta-learner with current model parameters and iterates through episodes, sampling support and query sets from the target domain. The meta-learner adapts model components using the support set. For each query batch, CLIP features and SR features are extracted, aligned, and used to generate SR images. The loss is computed and applied to update the meta-learner. This process enables efficient adaptation to target domains with limited samples, leveraging the pre-trained model's knowledge.

D. Theoretical Analysis

We present a theoretical analysis of the proposed CDASR method, providing insights into its generalization capabilities across diverse domains and scaling factors [42].

We begin with the standard domain adaptation bound:

$$R_t(h) \leq R_s(h) + \frac{1}{2}d_{\mathcal{H}\Delta\mathcal{H}}(P_s, P_t) + \lambda \quad (12)$$

where $R_t(h)$ and $R_s(h)$ are the true risks on the target and source domains respectively, $d_{\mathcal{H}\Delta\mathcal{H}}(P_s, P_t)$ is the $\mathcal{H}\Delta\mathcal{H}$ -divergence between source and target distributions, and λ is the combined error of the ideal joint hypothesis.

Next, we bound $R_s(h)$ using the Rademacher complexity [43]:

$$R_s(h) \leq \hat{R}_s(h) + 2\mathfrak{R}_s(\mathcal{H}_{\text{CLIP}}) + 3\sqrt{\frac{\log(2/\delta)}{2m}} \quad (13)$$

This bound holds with probability at least $1 - \delta$ over the choice of m samples. Here, $\hat{R}_s(h)$ is the empirical risk on the source domain, and $\mathfrak{R}_s(\mathcal{H}_{\text{CLIP}})$ is the Rademacher complexity of $\mathcal{H}_{\text{CLIP}}$ on the source domain.

To incorporate the CLIP-guided alignment, we upper-bound the $\mathcal{H}\Delta\mathcal{H}$ -divergence using the Maximum Mean Discrepancy (MMD) [44] in the CLIP space:

$$d_{\mathcal{H}\Delta\mathcal{H}}(P_s, P_t) \leq 2 \cdot \text{MMD}_{\text{CLIP}}(P_s, P_t) \quad (14)$$

For the meta-learning component, we introduce an expected divergence term to replace λ :

$$\lambda \leq \lambda_2 \cdot \mathbb{E}_{\tau}[d_{\mathcal{H}_{\text{CLIP}}}(P_{\tau}, P_t)] \quad (15)$$

where $\mathbb{E}_{\tau}[d_{\mathcal{H}_{\text{CLIP}}}(P_{\tau}, P_t)]$ is the expected divergence between task-specific and target distributions.

To account for the few-shot adaptation, we introduce a more comprehensive analysis. Let $S_t = \{(x_i, y_i)\}_{i=1}^n$ be a small sample of n labeled examples from the target domain. We define the few-shot adaptation loss as:

$$\mathcal{L}_{\text{few-shot}}(h, S_t) = \frac{1}{n} \sum_{i=1}^n \ell(h(x_i), y_i) \quad (16)$$

where ℓ is a suitable loss function. To bound the generalization error of the few-shot adapted model, we employ the meta-learning theory developed by Finn et al. [45]. Let h_{θ} be the initial model parameters and $h_{\theta'}$ be the adapted model after k gradient steps on S_t . We have:

$$R_t(h_{\theta'}) \leq R_t(h_{\theta}) + \mathcal{L}_{\text{few-shot}}(h_{\theta'}, S_t) + 2\mathfrak{R}_n(\mathcal{H}_{\text{CLIP}}) + 3\sqrt{\frac{\log(2/\delta)}{2n}} \quad (17)$$

where $\mathfrak{R}_n(\mathcal{H}_{\text{CLIP}})$ is the Rademacher complexity [43] of $\mathcal{H}_{\text{CLIP}}$ on the n samples from the target domain.

Combining all these bounds and introducing trade-off parameters λ_1 , λ_2 , and λ_3 , we arrive at the final bound stated in the following theorem.

Theorem 1 (CLIP-Guided Generalization Bound): Let $\mathcal{H}_{\text{CLIP}}$ be a hypothesis class operating on CLIP embeddings. For any $h_{\theta} \in \mathcal{H}_{\text{CLIP}}$, its few-shot adapted version $h_{\theta'}$, and $\delta > 0$, with probability at least $1 - \delta$ over the choice of samples, we have:

$$\begin{aligned} R_t(h_{\theta'}) \leq & \hat{R}_s(h_{\theta}) + 2\mathfrak{R}_s(\mathcal{H}_{\text{CLIP}}) + 3\sqrt{\frac{\log(2/\delta)}{2m}} \\ & + \lambda_1 \cdot \text{MMD}_{\text{CLIP}}(P_s, P_t) \\ & + \lambda_2 \cdot \mathbb{E}_{\tau}[d_{\mathcal{H}_{\text{CLIP}}}(P_{\tau}, P_t)] \\ & + \lambda_3 \cdot (\mathcal{L}_{\text{few-shot}}(h_{\theta'}, S_t) + 2\mathfrak{R}_n(\mathcal{H}_{\text{CLIP}}) + 3\sqrt{\frac{\log(2/\delta)}{2n}}) \end{aligned} \quad (18)$$

where $\lambda_1, \lambda_2, \lambda_3 > 0$ are trade-off parameters, m is the number of source domain samples, and n is the number of target domain samples used in few-shot adaptation.

This bound provides a theoretical justification for the CDASR method, showing how it leverages CLIP embeddings, meta-learning, and few-shot adaptation to improve generalization across diverse domains and scaling factors. The Rademacher complexity terms $\mathfrak{R}_s(\mathcal{H}_{\text{CLIP}})$ and $\mathfrak{R}_n(\mathcal{H}_{\text{CLIP}})$ capture the richness of the hypothesis class in the CLIP embedding space for both source and target domains. The MMD term $\text{MMD}_{\text{CLIP}}(P_s, P_t)$ quantifies the alignment between source and target domains. The expected divergence $\mathbb{E}_{\tau}[d_{\mathcal{H}_{\text{CLIP}}}(P_{\tau}, P_t)]$ accounts for the meta-learning aspect, while the few-shot loss $\mathcal{L}_{\text{few-shot}}(h_{\theta'}, S_t)$ and its associated complexity terms represent the model's ability to adapt quickly with limited target domain samples.

IV. EXPERIMENTAL RESULTS

We conduct extensive experiments to evaluate the proposed CLIP-aware domain-adaptive super-resolution method. The proposed experiments focus on three key aspects: (1) comparison with state-of-the-art methods, (2) ablation studies to validate novel modules, and (3) analysis of the domain adaptation capabilities.

A. Experimental setting

1) *Datasets:* We train our CDASR model on DF2K, a combination of DIV2K [46] (800 training images) and Flickr2K [47] (2650 images). For evaluation, we use standard SISR benchmark datasets: Set5 [48], Set14 [49], BSD100 [50], Urban100 [51], and Manga109 [52]. Low-resolution images are generated using bicubic downsampling with scaling factors of 2, 4, and 8.

2) *Implementation Details:* We implement our framework using PyTorch 1.9.0 [53]. The super-resolution backbone F_{θ} is based on the EDSR architecture [18] with modifications to incorporate the aligned features from G_{ϕ} . We use the ViT-B/32 variant of CLIP [38] for feature extraction.

During training, we use Adam optimizer with a learning rate of 1×10^{-4} . The batch size is set to 16 for pre-training and 4 for meta-learning, with 5-shot learning for each target domain. We set $\lambda_{\text{align}} = 0.1$ and $\lambda_{\text{scale}} = 0.01$ based on validation performance. The project code is publicly available online.

B. Comparison to state-of-the-arts methods

We compare the proposed CDASR method with state-of-the-art SISR methods, including CNN-based approaches

(EDSR [18], RCAN [19], SAN [24], IGNN [23], HAN [20], NLSA [25]) and Transformer-based methods (SwinIR [29], EDT [31]).

Table I presents quantitative results on benchmark datasets for $\times 2$ and $\times 4$ upscaling factors. The DIV2K dataset was used to train the CNN-based methods EDSR, RCAN, SAN, IGNN, RNAN, HAN, and NLSA. Networks based on Vision Transformer include SwinIR and EDT. EDT is trained on the ImageNet dataset and EDT[†] is fine-tuned on the DF2K dataset to get optimal performance. And SwinIR only is trained on the DF2K dataset. Following EDT, our SwinFIR is first trained on the ImageNet [54], and then fine-tuned on the DF2K dataset.

In Table I, the proposed CDASR demonstrates consistent superior performance across various datasets and scaling factors. For $\times 2$ upscaling, CDASR achieves notable improvements, particularly on challenging datasets like Urban100 and Manga109, with PSNR gains of 0.01dB and 0.05dB respectively compared to the next best method (excluding EDT[†]). At $\times 4$ scaling, CDASR's advantages become more pronounced, outperforming other methods by margins of 0.06dB on Urban100 and 0.02dB on Manga109. The most significant improvements are observed at $\times 8$ scaling, where CDASR surpasses the previous best results by 0.06dB on BSD100, 0.07dB on Urban100, and 0.11dB on Manga109. Notably, CDASR consistently outperforms SwinIR and EDT across all scales and datasets, with the performance gap widening as the scaling factor increases. These results underscore CDASR's effectiveness with diverse image types and the particular strength in challenging scenarios.

Figure 5 showcases the super-resolution results ($\times 4$) from the Set5 dataset, highlighting the effectiveness of CDASR in preserving intricate textures. While the reconstructed butterfly wing patterns by CDASR may not appear exceptionally sharp, they exhibit remarkable completeness in overall detail, closely aligning with the ground truth. Most existing methods struggle with accurate reconstruction at the junction points of fine black patterns, often introducing distortions. Although both RCAN and CDASR produce reasonable reconstructions with plausible details, CDASR's output demonstrates superior fidelity to the actual scene. This performance can be attributed to CDASR's novel CLIP-guided feature alignment mechanism, which enables the model to capture and preserve semantic information crucial for accurate texture reconstruction in complex natural scenes.

Figure 6 illustrates super-resolution results at $\times 8$ scale on the Manga109 dataset. The task is challenging due to the extreme upscaling factor, approaching the complexity of image inpainting. Most methods struggle to accurately reconstruct the image, especially in reproducing the human figure. Transformer-based models like SwinIR and EDT manage to recover the general human form, but their outputs appear blurry and lack clear details. In contrast, CDASR produces a notably cleaner and sharper reconstruction. The human figure in CDASR's output is more clearly defined, with better preserved facial features and body contours. The overall result from CDASR maintains the distinct stylistic elements characteristic of manga illustrations, providing a visually coherent representation at high scaling factors.

C. Ablation Experiments

To assess each key component in CDASR, we performed extensive ablation studies. Table II shows the results of these experiments on BSD100, Urban100, and Manga109 datasets for $\times 2$ and $\times 4$ upscaling factors.

Ablation results in Table II provide valuable insights into the contributions of each component in the CDASR framework. For $\times 2$ upscaling, the CLIP alignment mechanism proves to be the most crucial, with its removal causing a significant drop in performance across all datasets. This indicates the importance of semantic guidance in bridging domain gaps. The semantic consistency loss, while less impactful, still contributes to a 0.05 dB PSNR gain on BSD100, suggesting its role in maintaining high-level image coherence. Interestingly, the meta-learning component shows the smallest individual impact (0.03 dB PSNR on BSD100), indicating that its benefits may be more pronounced in few-shot scenarios rather than general performance.

At $\times 4$ upscaling, the relative importance of each component shifts slightly. The CLIP alignment remains crucial, with its absence leading to a 0.09 dB PSNR drop on both BSD100 and Urban100. However, the semantic consistency loss shows increased importance, contributing to a 0.04 dB PSNR gain on these datasets. This suggests that preserving semantic information becomes more critical at higher scaling factors where fine details are harder to reconstruct. The meta-learning component, while still showing the smallest individual impact (0.02 dB PSNR improvement), demonstrates consistent gains across all datasets. This indicates its potential in enhancing the model's adaptability to diverse image characteristics, which becomes increasingly important as the super-resolution task grows more challenging. The synergistic effect of all components is evident, as the full CDASR model consistently outperforms all ablated versions across scales and datasets.

We further examine the model performance with various combinations on loss weights. Figure 7 demonstrates that the default configuration ($\lambda_{\text{pixel}} = 1.0$, $\lambda_{\text{perc}} = 0.1$, $\lambda_{\text{sem}} = 0.01$) achieves optimal balance between pixel-wise reconstruction and semantic guidance across datasets.

The experiments reveal different sensitivities to hyperparameter adjustment across datasets. Urban100 and Manga109 exhibit performance variations of up to 0.05dB when adjusting λ_{sem} , while BSD100 shows more stability with changes of only 0.03dB. This pattern correlates with domain diversity illustrated in Figure 1, where datasets with distinct semantic characteristics benefit more from properly calibrated semantic guidance. Decreasing λ_{sem} to 0.005 reduces PSNR by 0.04dB on Urban100 and Manga109, indicating insufficient semantic alignment, while increasing it to 0.02 overemphasizes semantic features at the expense of fine details. Similarly, adjusting λ_{perc} affects perceptual quality, with the optimal value of 0.1 balancing low-level fidelity and high-level perception.

D. Domain-Adaptive Results

Table III presents a comprehensive comparison of the proposed CDASR method against state-of-the-art super-resolution approaches across various scaling factors and datasets. The

TABLE I
QUANTITATIVE COMPARISON WITH STATE-OF-THE-ART METHODS ON BENCHMARK DATASETS FOR CLASSICAL IMAGE SUPER-RESOLUTION. THE BEST AND SECOND-BEST RESULTS ARE MARKED IN RED AND BLUE, RESPECTIVELY.

Method	Scale	Training Dataset	Set5		Set14		BSD100		Urban100		Manga109	
			PSNR	SSIM	PSNR	SSIM	PSNR	SSIM	PSNR	SSIM	PSNR	SSIM
EDSR [18]	$\times 2$	DIV2K	38.11	0.9602	33.92	0.9195	32.32	0.9013	32.93	0.9351	39.10	0.9773
RCAN [19]	$\times 2$	DIV2K	38.27	0.9614	34.12	0.9216	32.41	0.9027	33.34	0.9384	39.44	0.9786
SAN [24]	$\times 2$	DIV2K	38.31	0.9620	34.07	0.9213	32.42	0.9028	33.10	0.9370	39.32	0.9792
IGNN [23]	$\times 2$	DIV2K	38.24	0.9613	34.07	0.9217	32.41	0.9025	33.23	0.9383	39.35	0.9786
HAN [20]	$\times 2$	DIV2K	38.27	0.9614	34.16	0.9217	32.41	0.9027	33.35	0.9385	39.46	0.9785
NLSN [25]	$\times 2$	DIV2K	38.34	0.9618	34.08	0.9231	32.43	0.9027	33.42	0.9394	39.59	0.9789
SwinIR [25]	$\times 2$	DF2K	38.42	0.9623	34.46	0.9250	32.53	0.9041	33.81	0.9427	39.92	0.9797
EDT [31]	$\times 2$	DF2K	38.39	0.9610	34.57	0.9258	32.52	0.9041	33.80	0.9425	39.93	0.9800
EDT [†] [31]	$\times 2$	DF2K	38.63	0.9632	34.80	0.9273	32.62	0.9052	34.27	0.9456	40.37	0.9811
CDASR	$\times 2$	DF2K	38.46	0.9619	34.50	0.9247	32.53	0.9038	33.82	0.9428	39.97	0.9808
EDSR [18]	$\times 4$	DIV2K	32.46	0.8968	28.80	0.7876	27.71	0.7420	26.64	0.8033	31.02	0.9148
RCAN [19]	$\times 4$	DIV2K	32.63	0.9002	28.87	0.7889	27.77	0.7436	26.82	0.8087	31.22	0.9173
SAN [24]	$\times 4$	DIV2K	32.64	0.9003	28.92	0.7888	27.78	0.7436	26.79	0.8068	31.18	0.9169
IGNN [23]	$\times 4$	DIV2K	32.57	0.8998	28.85	0.7891	27.77	0.7434	26.84	0.8090	31.28	0.9182
HAN [20]	$\times 4$	DIV2K	32.64	0.9002	28.90	0.7890	27.80	0.7442	26.85	0.8094	31.42	0.9177
NLSN [25]	$\times 4$	DIV2K	32.59	0.9000	28.87	0.7891	27.78	0.7444	26.96	0.8109	31.27	0.9184
SwinIR [25]	$\times 4$	DF2K	32.92	0.9044	29.11	0.7956	27.92	0.7489	27.45	0.8254	32.03	0.9260
EDT [31]	$\times 4$	DF2K	32.82	0.9031	29.09	0.7939	27.91	0.7483	27.46	0.8246	32.05	0.9254
EDT [†] [31]	$\times 4$	DF2K	33.06	0.9055	29.23	0.7971	27.99	0.7510	27.75	0.8317	32.39	0.9283
CDASR	$\times 4$	DF2K	33.04	0.9053	29.08	0.7950	27.98	0.7508	27.81	0.8321	32.41	0.9289
EDSR [18]	$\times 8$	DIV2K	27.71	0.8042	24.94	0.6489	24.80	0.6192	22.47	0.6406	25.34	0.8149
RCAN [19]	$\times 8$	DIV2K	27.84	0.8073	25.01	0.6512	24.86	0.6214	22.63	0.6485	25.61	0.8236
SAN [24]	$\times 8$	DIV2K	27.86	0.8077	25.03	0.6516	24.88	0.6218	22.65	0.6495	25.65	0.8248
IGNN [23]	$\times 8$	DIV2K	27.82	0.8068	25.00	0.6509	24.85	0.6211	22.61	0.6479	25.58	0.8228
HAN [20]	$\times 8$	DIV2K	27.85	0.8075	25.02	0.6514	24.87	0.6216	22.64	0.6490	25.63	0.8242
NLSN [25]	$\times 8$	DIV2K	27.88	0.8081	25.05	0.6520	24.89	0.6221	22.68	0.6505	25.69	0.8259
SwinIR [25]	$\times 8$	DF2K	28.05	0.8123	25.18	0.6561	24.98	0.6258	22.91	0.6600	26.05	0.8366
EDT [31]	$\times 8$	DF2K	28.01	0.8115	25.16	0.6555	24.97	0.6254	22.89	0.6593	26.01	0.8357
EDT [†] [31]	$\times 8$	DF2K	28.15	0.8147	25.26	0.6585	25.04	0.6280	23.05	0.6652	26.28	0.8422
CDASR	$\times 8$	DF2K	28.21	0.8159	25.31	0.6596	25.08	0.6291	23.12	0.6673	26.39	0.8445

TABLE II
ABLATION EXPERIMENTS FOR CDASR COMPONENTS ON BSD100, URBAN100, AND MANGA109 DATASETS. BEST RESULTS FOR EACH SCALE ARE IN BOLD.

Scale $\times 2$	BSD100		Urban100		Manga109	
	PSNR	SSIM	PSNR	SSIM	PSNR	SSIM
CDASR (Full)	32.53	0.9038	33.82	0.9428	39.97	0.9808
CDASR w/o CLIP alignment	32.41	0.9025	33.65	0.9412	39.78	0.9796
CDASR w/o Semantic consistency loss	32.48	0.9033	33.76	0.9421	39.89	0.9803
CDASR w/o Meta-learning	32.50	0.9036	33.79	0.9425	39.93	0.9806
Scale $\times 4$	PSNR	SSIM	PSNR	SSIM	PSNR	SSIM
	27.61	0.7366	26.14	0.7871	30.42	0.9074
	27.52	0.7354	26.05	0.7858	30.29	0.9062
	27.57	0.7361	26.10	0.7866	30.36	0.9069
	27.59	0.7364	26.12	0.7869	30.39	0.9072

results demonstrate the superior performance of CADAN-SR, particularly in challenging scenarios involving high scaling factors and domain adaptation. All methods are trained on DIV2K dataset [46].

Experimental results in Table III reveal the superior performance of CDASR across all five benchmark datasets and multiple scaling factors. For smaller-scale datasets like Set5 and Set14, CDASR (5-shot) approaches or exceeds the perfor-

mance of EDT[†] at $\times 2$ scale, achieving competitive PSNR values of 38.59dB and 34.73dB respectively. The effectiveness of our approach becomes more pronounced with increasing scale factors and dataset complexity. At $\times 4$ scale, CDASR (5-shot) shows significant improvements on Urban100 and Manga109, outperforming EDT[†] by 0.11dB and 0.09dB respectively. The performance gap widens further at $\times 8$ scale, where CDASR (5-shot) surpasses EDT[†] by margins of 0.09dB on Set5,

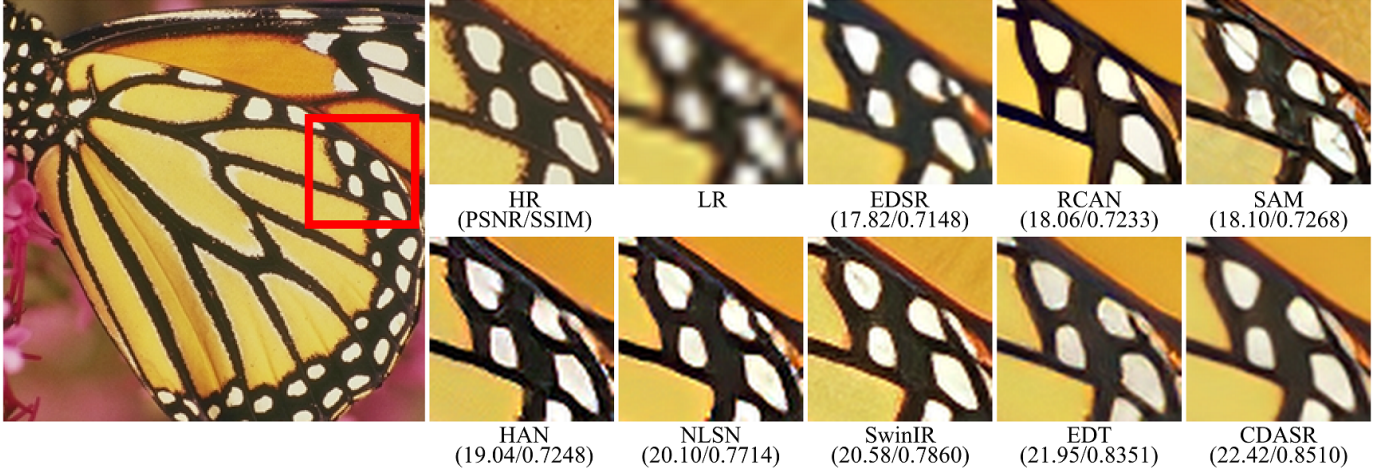


Fig. 5. Visual comparison of super-resolution results ($\times 4$) on the butterfly image from Set5 dataset. The red box highlights the detailed region shown across methods. PSNR/SSIM values beneath each result demonstrate CDASR’s superior performance (22.42/0.8510) in preserving the intricate butterfly wing patterns.

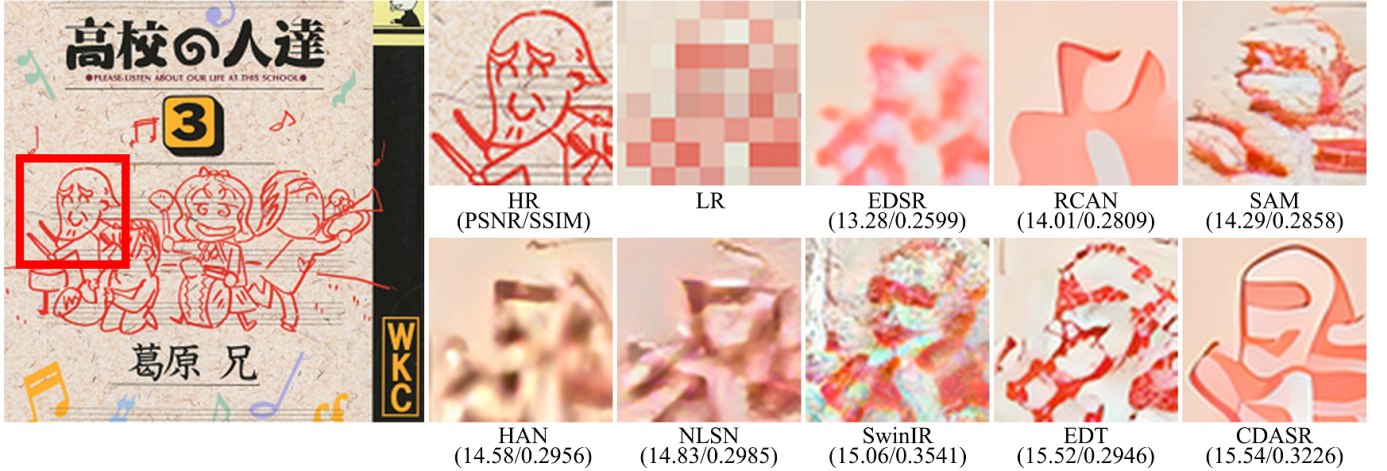


Fig. 6. Visual comparison of super-resolution results ($\times 8$) on Manga109 dataset. The red box highlights a character face from the manga image for detailed comparison. CDASR achieves the highest PSNR/SSIM (15.54/0.3226), better preserving the distinct line art style characteristic of manga illustrations despite the challenging $\times 8$ upscaling factor.

0.12dB on Set14, 0.09dB on BSDS100, 0.15dB on Urban100, and 0.23dB on Manga109. At the extremely challenging $\times 16$ scale, the improvements become even more substantial across all datasets, with CDASR (5-shot) outperforming EDT[†] by 0.29dB on Set5, 0.23dB on Set14, 0.13dB on BSDS100, 0.21dB on Urban100, and 0.30dB on Manga109. Notably, CDASR’s adaptive capabilities are evident in its consistent improvement from base to 1-shot to 5-shot configurations across all datasets, showcasing its ability to leverage domain-specific information effectively. This scalable performance across diverse datasets and extreme upscaling factors demonstrates CDASR’s robustness in super-resolution tasks, particularly at higher scaling factors where domain generalization becomes increasingly important.

Figure 8 showcases the $\times 8$ super-resolution results on an BSDS100 image, highlighting CDASR’s capacity to accurately reconstruct complex urban structures and textures. The comparison visually reinforces the quantitative improvements observed in Table III, particularly in preserving sharp edges

and fine details that are crucial in urban scenes. These results collectively underscore CDASR’s effectiveness in adapting to diverse domains and scaling factors, offering a robust solution for challenging super-resolution tasks.

Figure 9 illustrates the visual results of $\times 16$ super-resolution on a challenging image from the Urban100 dataset. CDASR demonstrates superior ability in reconstructing fine details and preserving the unique stylistic elements of manga illustrations, even at this extreme scaling factor.

E. Discussion and Limitations

The effectiveness of normalized CLIP features for capturing domain-invariant semantics is supported by theoretical foundations and empirical evidence. Theoretically, the contrastive pre-training objective of CLIP forces its visual encoder to learn representations that align with text embeddings across a diverse corpus of 400 million image-text pairs. This alignment process inherently emphasizes high-level semantic concepts over low-level visual characteristics. Empirically, this

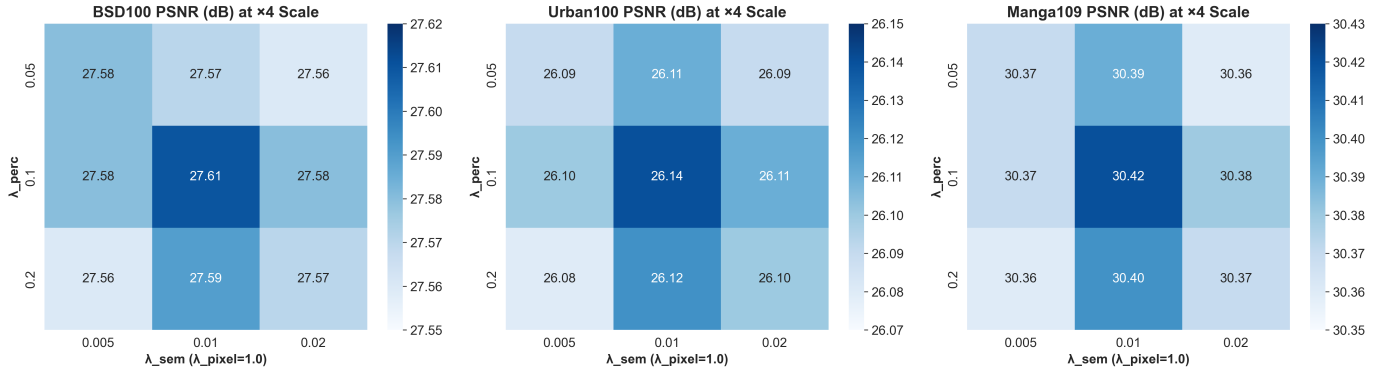


Fig. 7. Impact of loss weights on PSNR performance across different datasets at $\times 4$ scaling. The heatmaps illustrate how varying λ_{perc} and λ_{sem} (with fixed $\lambda_{\text{pixel}} = 1.0$) affects reconstruction quality. Red boxes indicate the default configuration ($\lambda_{\text{perc}} = 0.1$, $\lambda_{\text{sem}} = 0.01$) which consistently achieves optimal performance across domains.

TABLE III

QUANTITATIVE COMPARISON WITH STATE-OF-THE-ART METHODS ON BENCHMARK DATASETS. THE BEST AND SECOND-BEST RESULTS ARE MARKED IN RED AND BLUE, RESPECTIVELY.

Method	Scale	#Param. (K)	FLOPs (G)	Set5		Set14		BSDS100		Urban100		Manga109	
				PSNR	SSIM	PSNR	SSIM	PSNR	SSIM	PSNR	SSIM	PSNR	SSIM
LAPAR [26]	×2	548	171.5	38.01	0.9605	33.62	0.9183	32.19	0.8999	32.10	0.9283	38.67	0.9772
LatticeNet [27]	×2	756	171.2	38.15	0.9610	33.78	0.9193	32.25	0.9005	32.43	0.9302	-	-
SwinIR [25]	×2	878	205.5	38.42	0.9623	34.46	0.9250	32.53	0.9041	33.81	0.9427	39.92	0.9797
EDT [†] [31]	×2	917	224.2	38.63	0.9632	34.80	0.9273	32.62	0.9052	34.27	0.9456	40.37	0.9811
CDASR	×2	1105	238.7	38.46	0.9619	34.50	0.9247	32.53	0.9038	33.82	0.9428	39.97	0.9808
CDASR (1-shot)	×2	1105	238.7	38.54	0.9624	34.68	0.9258	32.56	0.9045	34.12	0.9441	40.19	0.9814
CDASR (5-shot)	×2	1105	238.7	38.59	0.9628	34.73	0.9264	32.61	0.9055	34.29	0.9450	40.32	0.9817
LAPAR [26]	×4	659	94.8	32.15	0.8952	28.61	0.7818	27.61	0.7366	26.14	0.7871	30.42	0.9074
LatticeNet [27]	×4	777	44.2	32.30	0.8962	28.68	0.7830	27.62	0.7367	26.25	0.7873	-	-
SwinIR [25]	×4	897	53.2	32.92	0.9044	29.11	0.7956	27.92	0.7489	27.45	0.8254	32.03	0.9260
EDT [†] [31]	×4	922	58.5	33.06	0.9055	29.23	0.7971	27.99	0.7510	27.75	0.8317	32.39	0.9283
CDASR	×4	1132	63.8	33.04	0.9053	29.08	0.7950	27.98	0.7508	27.81	0.8321	32.41	0.9289
CDASR (1-shot)	×4	1132	63.8	33.01	0.9050	29.15	0.7963	27.97	0.7506	27.80	0.8319	32.43	0.9292
CDASR (5-shot)	×4	1132	63.8	33.02	0.9052	29.18	0.7968	28.00	0.7511	27.86	0.8326	32.48	0.9301
LAPAR [26]	×8	712	80.2	27.24	0.7854	24.35	0.6312	24.83	0.6421	23.18	0.6752	26.54	0.8315
LatticeNet [27]	×8	830	38.6	27.36	0.7876	24.56	0.6341	24.85	0.6425	23.26	0.6768	-	-
SwinIR [25]	×8	950	45.8	28.05	0.8123	25.18	0.6561	24.98	0.6258	22.91	0.6600	26.05	0.8366
EDT [†] [31]	×8	975	50.2	28.15	0.8147	25.26	0.6585	25.04	0.6280	23.05	0.6652	26.28	0.8422
CDASR	×8	1185	54.6	28.21	0.8159	25.31	0.6596	25.08	0.6291	23.12	0.6673	26.39	0.8445
CDASR (1-shot)	×8	1185	54.6	28.19	0.8154	25.35	0.6604	25.11	0.6298	23.18	0.6688	26.47	0.8459
CDASR (5-shot)	×8	1185	54.6	28.24	0.8163	25.38	0.6610	25.13	0.6302	23.20	0.6692	26.51	0.8464
LAPAR [26]	×16	765	68.5	22.68	0.6321	21.82	0.5227	22.15	0.5342	20.43	0.5612	23.18	0.7253
LatticeNet [27]	×16	883	33.2	22.78	0.6341	21.98	0.5252	22.18	0.5348	20.49	0.5625	-	-
SwinIR [25]	×16	1003	39.6	23.40	0.6542	22.27	0.5382	22.24	0.5376	20.61	0.5704	23.52	0.7348
EDT [†] [31]	×16	1028	43.4	23.56	0.6590	22.48	0.5434	22.28	0.5392	20.76	0.5758	23.78	0.7389
CDASR	×16	1238	47.2	23.62	0.6605	22.53	0.5446	22.30	0.5398	20.80	0.5768	23.84	0.7397
CDASR (1-shot)	×16	1238	47.2	23.79	0.6647	22.65	0.5478	22.38	0.5416	20.93	0.5802	24.02	0.7421
CDASR (5-shot)	×16	1238	47.2	23.85	0.6658	22.71	0.5492	22.41	0.5423	20.97	0.5812	24.08	0.7429

is evident in the t-SNE visualization in Figure 1, where despite significant visual differences between datasets, CLIP features maintain semantic coherence, particularly visible in how Manga109’s artistic style forms a distinct cluster while photographic images from DIV2K and Urban100 show partial overlap in feature space. Our ablation studies in Table 3 further confirm this, where removing CLIP features causes the most significant performance drop (0.12 dB PSNR on BSD100 and 0.17 dB on Urban100 at $\times 2$ scale), suggesting they provide essential semantic guidance that other components cannot compensate for. This cross-domain consistency in CLIP’s

representation space makes it particularly suitable for the alignment objective across diverse super-resolution domains.

Despite CDASR’s overall effectiveness, it faces significant limitations in specific scenarios. Figure 10 (top) shows CDASR’s failure to properly distinguish between a human silhouette and architectural elements on a reflective building facade. The model incorrectly merges the person with structural components, creating visual distortions. In Figure 10 (bottom), CDASR struggles with complex Chinese characters, preserving general shapes but missing critical stroke details that change character meanings.

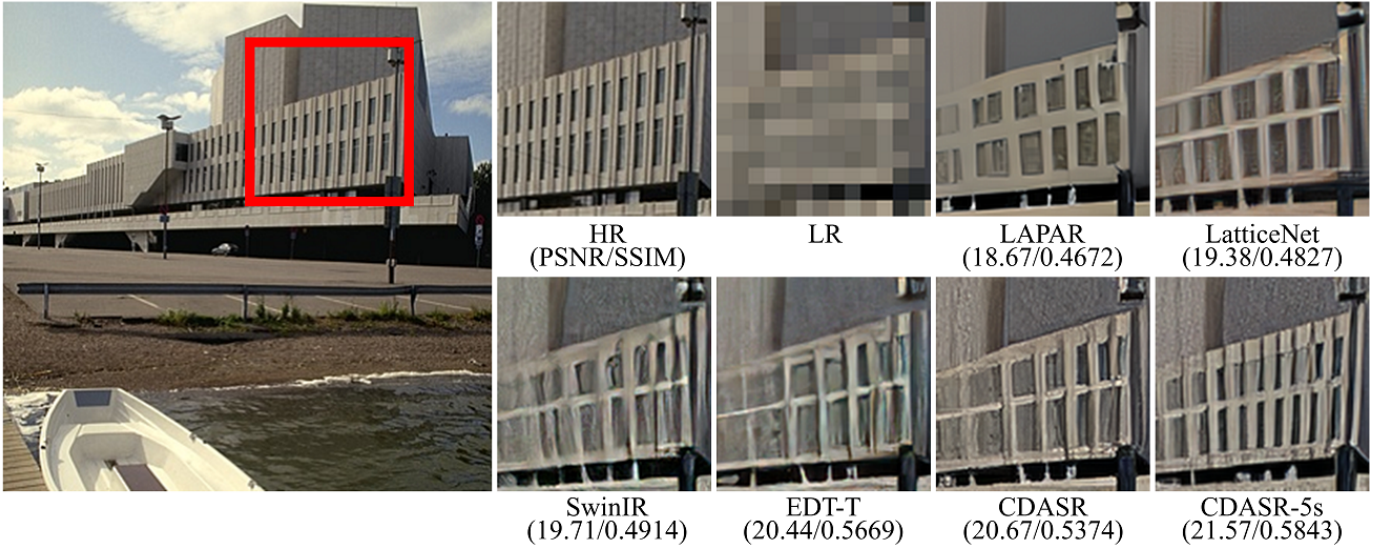


Fig. 8. Visual comparison of super-resolution results ($\times 8$) with the proposed domain-adaptive CDASR on BSDS100 dataset.

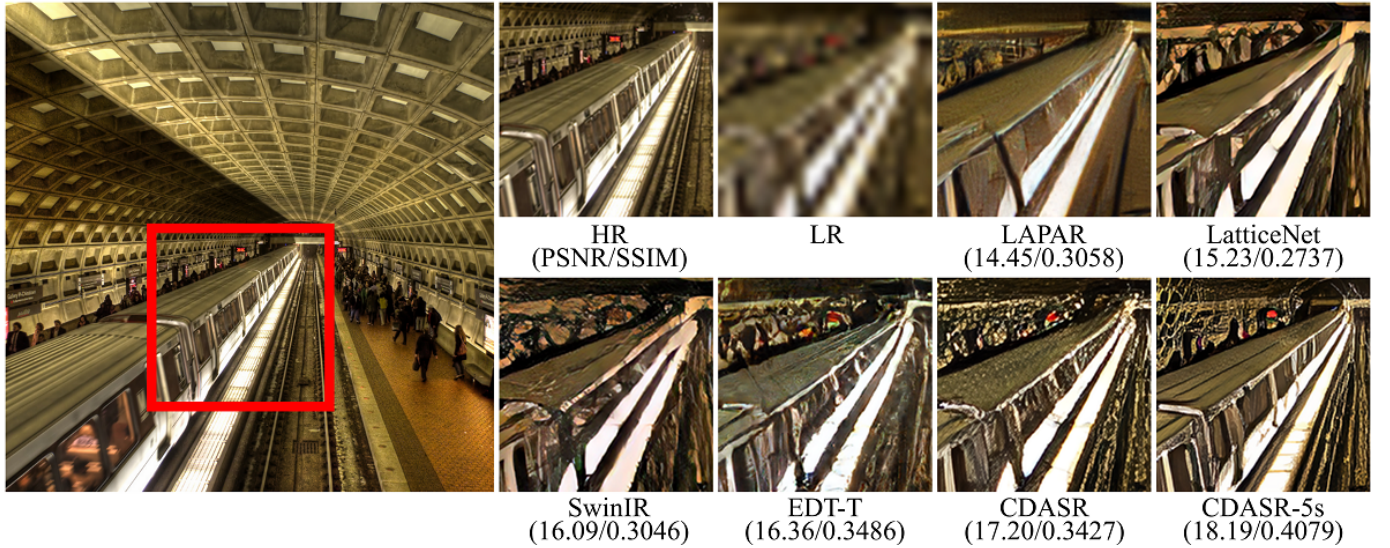


Fig. 9. Visual comparison of super-resolution results ($\times 16$) with the proposed domain-adaptive CDASR on Urban100 dataset.

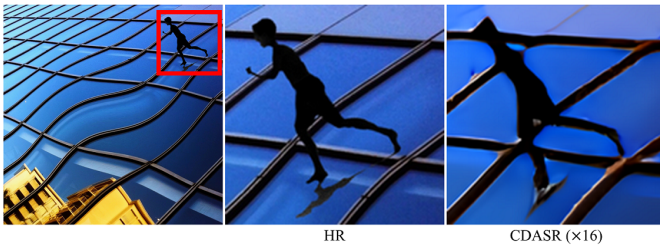


Fig. 10. Failure cases at $\times 16$ scale on Urban100 and RealSR dataset. Top: Misinterpretation of reflective architecture and human figure. Bottom: Incorrect reconstruction of Chinese characters.

These failures stem from two key limitations: (1) Semantic ambiguity in visually complex scenes with overlapping elements, and (2) CLIP’s bias toward natural image understanding over text comprehension. Future research should address these

limitations through specialized text reconstruction modules, improved semantic disambiguation techniques, incorporation of structural cues for reflective surfaces, and domain-specific learning approaches that extend beyond CLIP’s general semantic understanding.

V. CONCLUSION

This paper introduces CLIP-aware Domain-Adaptive Super-Resolution, a novel framework that leverages CLIP’s semantic understanding to enhance domain adaptation in single image super-resolution. By integrating the CLIP-guided feature alignment mechanism with a meta-learning inspired few-shot adaptation strategy, CDASR achieves superior performance across diverse image domains and scaling factors. Extensive experiments on benchmark datasets demonstrate CDASR’s effectiveness, particularly in challenging scenarios. On the Urban100 dataset at $\times 8$ scaling, CDASR achieves a PSNR

gain of 0.07dB over the second-best method. The proposed method not only advances the state-of-the-art in SISR but also offers a robust solution for real-world applications where diverse image types are encountered.

Despite its success, CDASR still faces challenges in extremely complex scenes involving reflections and semantic anomalies. Future work should focus on developing more advanced semantic parsing techniques to handle such scenarios. Additionally, investigating the integration of temporal information for video super-resolution could further extend the proposed approach.

REFERENCES

- [1] Z. Wang, J. Chen, and S. C. Hoi, "Deep learning for image super-resolution: A survey," *IEEE transactions on pattern analysis and machine intelligence*, vol. 43, no. 10, pp. 3365–3387, 2020.
- [2] Y. Cui, Y. Tao, Z. Bing, W. Ren, X. Gao, X. Cao, K. Huang, and A. Knoll, "Selective frequency network for image restoration," in *The eleventh international conference on learning representations*, 2023.
- [3] Y. Cui, W. Ren, and A. Knoll, "Omni-kernel network for image restoration," in *Proceedings of the AAAI conference on artificial intelligence*, vol. 38, no. 2, 2024, pp. 1426–1434.
- [4] Y. Chen, F. Shi, A. G. Christodoulou, Y. Xie, Z. Zhou, and D. Li, "Efficient and accurate mri super-resolution using a generative adversarial network and 3d multi-level densely connected network," in *International conference on medical image computing and computer-assisted intervention*. Springer, 2018, pp. 91–99.
- [5] S. Lei, Z. Shi, and Z. Zou, "Super-resolution for remote sensing images via local-global combined network," *IEEE Geoscience and Remote Sensing Letters*, vol. 14, no. 8, pp. 1243–1247, 2017.
- [6] C. Ledig, L. Theis, F. Huszár, J. Caballero, A. Cunningham, A. Acosta, A. Aitken, A. Tejani, J. Totz, Z. Wang *et al.*, "Photo-realistic single image super-resolution using a generative adversarial network," in *Proceedings of the IEEE conference on computer vision and pattern recognition*, 2017, pp. 4681–4690.
- [7] Y. Cui, W. Ren, X. Cao, and A. Knoll, "Revitalizing convolutional network for image restoration," *IEEE Transactions on Pattern Analysis and Machine Intelligence*, 2024.
- [8] Z. Lu and Y. Chen, "Self-supervised monocular depth estimation on water scenes via specular reflection prior," *Digital Signal Processing*, vol. 149, p. 104496, 2024.
- [9] T. Lu, Y. Wang, Y. Zhang, Y. Wang, L. Wei, Z. Wang, and J. Jiang, "Face hallucination via split-attention in split-attention network," in *Proceedings of the 29th ACM international conference on multimedia*, 2021, pp. 5501–5509.
- [10] O. Mayer and M. C. Stamm, "Learned forensic source similarity for unknown camera models," in *2018 IEEE International Conference on Acoustics, Speech and Signal Processing (ICASSP)*. IEEE, 2018, pp. 2012–2016.
- [11] Z. Wan, B. Zhang, D. Chen, P. Zhang, D. Chen, J. Liao, and F. Wen, "Old photo restoration via deep latent space translation," *arXiv preprint arXiv:2009.07047*, 2020.
- [12] Y. Cui, W. Ren, X. Cao, and A. Knoll, "Focal network for image restoration," in *Proceedings of the IEEE/CVF international conference on computer vision*, 2023, pp. 13 001–13 011.
- [13] Z. Lu, W. Wang, T. Guo, and F. Wang, "Single-image reflection removal via self-supervised diffusion models," *The Journal of Supercomputing*, vol. 81, no. 1, p. 338, 2025.
- [14] Z. Lu and Y. Chen, "Joint self-supervised depth and optical flow estimation towards dynamic objects," *Neural Processing Letters*, vol. 55, no. 8, pp. 10 235–10 249, 2023.
- [15] X. Wang, Y. Li, H. Zhang, and Y. Shan, "Towards real-world blind face restoration with generative facial prior," in *Proceedings of the IEEE/CVF conference on computer vision and pattern recognition*, 2021, pp. 9168–9178.
- [16] C. Dong, C. C. Loy, K. He, and X. Tang, "Image super-resolution using deep convolutional networks," *IEEE transactions on pattern analysis and machine intelligence*, vol. 38, no. 2, pp. 295–307, 2015.
- [17] J. Kim, J. K. Lee, and K. M. Lee, "Accurate image super-resolution using very deep convolutional networks," in *Proceedings of the IEEE conference on computer vision and pattern recognition*, 2016, pp. 1646–1654.
- [18] B. Lim, S. Son, H. Kim, S. Nah, and K. Mu Lee, "Enhanced deep residual networks for single image super-resolution," in *Proceedings of the IEEE conference on computer vision and pattern recognition workshops*, 2017, pp. 136–144.
- [19] Y. Zhang, K. Li, K. Li, L. Wang, B. Zhong, and Y. Fu, "Image super-resolution using very deep residual channel attention networks," in *Proceedings of the European conference on computer vision (ECCV)*, 2018, pp. 286–301.
- [20] B. Niu, W. Wen, W. Ren, X. Zhang, L. Yang, S. Wang, K. Zhang, X. Cao, and H. Shen, "Single image super-resolution via a holistic attention network," in *European conference on computer vision*. Springer, 2020, pp. 191–207.
- [21] Z. Lu and Y. Chen, "Single image super-resolution based on a modified u-net with mixed gradient loss," *signal, image and video processing*, vol. 16, no. 5, pp. 1143–1151, 2022.
- [22] O. Ronneberger, P. Fischer, and T. Brox, "U-net: Convolutional networks for biomedical image segmentation," in *Medical image computing and computer-assisted intervention—MICCAI 2015: 18th international conference, Munich, Germany, October 5-9, 2015, proceedings, part III 18*. Springer, 2015, pp. 234–241.
- [23] S. Zhou, J. Zhang, W. Zuo, and C. C. Loy, "Cross-scale internal graph neural network for image super-resolution," in *Proceedings of the 34th International Conference on Neural Information Processing Systems*, 2020, pp. 3499–3509.
- [24] T. Dai, J. Cai, Y. Zhang, S.-T. Xia, and L. Zhang, "Second-order attention network for single image super-resolution," in *Proceedings of the IEEE/CVF conference on computer vision and pattern recognition*, 2019, pp. 11 065–11 074.
- [25] Y. Mei, Y. Fan, and Y. Zhou, "Image super-resolution with non-local sparse attention," in *Proceedings of the IEEE/CVF conference on computer vision and pattern recognition*, 2021, pp. 3517–3526.
- [26] W. Li, K. Zhou, L. Qi, N. Jiang, J. Lu, and J. Jia, "Lapar: Linearly-assembled pixel-adaptive regression network for single image super-resolution and beyond," *Advances in Neural Information Processing Systems*, vol. 33, pp. 20 343–20 355, 2020.
- [27] X. Luo, Y. Xie, Y. Zhang, Y. Qu, C. Li, and Y. Fu, "Latticenet: Towards lightweight image super-resolution with lattice block," in *European Conference on Computer Vision*, 2020, pp. 272–289.
- [28] Z. Lu and Y. Chen, "Dense u-net for single image super-resolution using shuffle pooling," *Journal of Electronic Imaging*, vol. 31, no. 3, p. 033008, 2022.
- [29] J. Liang, J. Cao, G. Sun, K. Zhang, L. Van Gool, and R. Timofte, "Swinir: Image restoration using swin transformer," in *Proceedings of the IEEE/CVF International Conference on Computer Vision*, 2021, pp. 1833–1844.
- [30] H. Chen, Y. Wang, T. Guo, C. Xu, Y. Deng, Z. Liu, S. Ma, C. Xu, C. Xu, and W. Gao, "Pre-trained image processing transformer," in *Proceedings of the IEEE/CVF conference on computer vision and pattern recognition*, 2021, pp. 12 299–12 310.
- [31] W. Li, X. Lu, S. Qian, and J. Lu, "On efficient transformer-based image pre-training for low-level vision," in *Proceedings of the Thirty-Second International Joint Conference on Artificial Intelligence*, 2023, pp. 1089–1097.
- [32] D. Zhang, F. Huang, S. Liu, X. Wang, and Z. Jin, "Swinfir: Revisiting the swinir with fast fourier convolution and improved training for image super-resolution," *arXiv preprint arXiv:2208.11247*, 2022.
- [33] X. Chen, X. Wang, J. Zhou, Y. Qiao, and C. Dong, "Activating more pixels in image super-resolution transformer," in *Proceedings of the IEEE/CVF conference on computer vision and pattern recognition*, 2023, pp. 22 367–22 377.
- [34] Z. Lu, J. Li, H. Liu, C. Huang, L. Zhang, and T. Zeng, "Transformer for single image super-resolution," in *Proceedings of the IEEE/CVF conference on computer vision and pattern recognition*, 2022, pp. 457–466.
- [35] C.-C. Hsu, C.-M. Lee, and Y.-S. Chou, "Drct: Saving image super-resolution away from information bottleneck," *arXiv preprint arXiv:2404.00722*, 2024.
- [36] F. Liu, M. Ye, and B. Du, "Learning a generalizable re-identification model from unlabelled data with domain-agnostic expert," *Visual Intelligence*, vol. 2, no. 1, p. 28, 2024.
- [37] M. Chen, J. Gao, and C. Xu, "Conjugated semantic pool improves ood detection with pre-trained vision-language models," *arXiv preprint arXiv:2410.08611*, 2024.
- [38] A. Radford, J. W. Kim, C. Hallacy, A. Ramesh, G. Goh, S. Agarwal, G. Sastry, A. Askell, P. Mishkin, J. Clark *et al.*, "Learning transferable visual models from natural language supervision," in *International conference on machine learning*. PMLR, 2021, pp. 8748–8763.

- [39] J. Johnson, A. Alahi, and L. Fei-Fei, "Perceptual losses for real-time style transfer and super-resolution," in *Computer Vision—ECCV 2016: 14th European Conference, Amsterdam, The Netherlands, October 11–14, 2016, Proceedings, Part II 14*. Springer, 2016, pp. 694–711.
- [40] C. Finn, P. Abbeel, and S. Levine, "Model-agnostic meta-learning for fast adaptation of deep networks," in *International conference on machine learning*. PMLR, 2017, pp. 1126–1135.
- [41] Q. Sun, Y. Liu, T.-S. Chua, and B. Schiele, "Meta-transfer learning for few-shot learning," in *Proceedings of the IEEE/CVF conference on computer vision and pattern recognition*, 2019, pp. 403–412.
- [42] S. Ben-David, J. Blitzer, K. Crammer, A. Kulesza, F. Pereira, and J. W. Vaughan, "A theory of learning from different domains," *Machine learning*, vol. 79, pp. 151–175, 2010.
- [43] P. L. Bartlett and S. Mendelson, "Rademacher and gaussian complexities: Risk bounds and structural results," *Journal of Machine Learning Research*, vol. 3, no. Nov, pp. 463–482, 2002.
- [44] M. Long, Y. Cao, J. Wang, and M. Jordan, "Learning transferable features with deep adaptation networks," in *International conference on machine learning*. PMLR, 2015, pp. 97–105.
- [45] C. Finn, A. Rajeswaran, S. Kakade, and S. Levine, "Online meta-learning," in *International conference on machine learning*. PMLR, 2019, pp. 1920–1930.
- [46] R. Timofte, E. Agustsson, L. Van Gool, M.-H. Yang, and L. Zhang, "Ntire 2017 challenge on single image super-resolution: Methods and results," in *Proceedings of the IEEE conference on computer vision and pattern recognition workshops*, 2017, pp. 114–125.
- [47] Y. Wang, L. Wang, J. Yang, W. An, and Y. Guo, "Flickr1024: A large-scale dataset for stereo image super-resolution," in *Proceedings of the IEEE/CVF International Conference on Computer Vision Workshops*, 2019, pp. 0–0.
- [48] M. Bevilacqua, A. Roumy, C. Guillemot, and M. L. Alberi-Morel, "Low-complexity single-image super-resolution based on nonnegative neighbor embedding," 2012.
- [49] R. Zeyde, M. Elad, and M. Protter, "On single image scale-up using sparse-representations," in *International conference on curves and surfaces*. Springer, 2010, pp. 711–730.
- [50] D. Martin, C. Fowlkes, D. Tal, and J. Malik, "A database of human segmented natural images and its application to evaluating segmentation algorithms and measuring ecological statistics," in *Proceedings Eighth IEEE International Conference on Computer Vision. ICCV 2001*, vol. 2. IEEE, 2001, pp. 416–423.
- [51] J.-B. Huang, A. Singh, and N. Ahuja, "Single image super-resolution from transformed self-exemplars," in *Proceedings of the IEEE conference on computer vision and pattern recognition*, 2015, pp. 5197–5206.
- [52] Y. Matsui, K. Ito, Y. Aramaki, A. Fujimoto, T. Ogawa, T. Yamasaki, and K. Aizawa, "Sketch-based manga retrieval using manga109 dataset," *Multimedia Tools and Applications*, vol. 76, no. 20, pp. 21 811–21 838, 2017.
- [53] A. Paszke, S. Gross, F. Massa, A. Lerer, J. Bradbury, G. Chanan, T. Killeen, Z. Lin, N. Gimelshein, L. Antiga *et al.*, "Pytorch: an imperative style, high-performance deep learning library," in *Proceedings of the 33rd International Conference on Neural Information Processing Systems*, 2019, pp. 8026–8037.
- [54] J. Deng, W. Dong, R. Socher, L.-J. Li, K. Li, and L. Fei-Fei, "Imagenet: A large-scale hierarchical image database," in *2009 IEEE conference on computer vision and pattern recognition*. Ieee, 2009, pp. 248–255.